Supplementary Information

Highly Efficient Nano-octahedral Au/γ-Fe₂O₃ Catalyst Synthesized by Dealloying Combined with Calcination for Low-Temperature CO Oxidation

Dong Duan[1, 2], Chunxi Hao[1, 2, *], Jiangang Jiang[1], and Ying Li[1]

[1] College of Science, Northwest A&F University, Yangling, Shaanxi, PR China, 712100.

[2] School of Physics, MOE Key Laboratory for Non-Equilibrium Synthesis and Modulation of Condensed Matter,

Xi'an Jiaotong University, Xi'an, Shaanxi, PR China, 710049.

* Corresponding author: Chunxi Hao; Email: haocx@nwafu.edu.cn.

Materials Characterization

The X-ray diffraction (XRD) patterns of the products were recorded on a Shimadzu XRD-6100 diffractometer (Japan) using copper Kα radiation (λ = 1.542 Å), with a scanning range of 20-80°, a scanning step length of 0.015°, and a scanning speed of 5°/min. The samples tested include Melt-spun $Al_{91.5}Fe_8Au_{0.5}$ ribbon; Au/γ-Fe_2O_3-Dealloyed; Au/γ-Fe_2O_3-400; γ-Fe_2O_3-400.

The Raman spectra of samples were measured on a HORIBA LabRAM HR Evolution Raman spectrometer (Japan) with an excitation laser source of 532 nm, covering the range from 250 cm^{-1} to 1800 cm^{-1}. The samples tested include Au/γ-Fe_2O_3-400 and γ-Fe_2O_3-400.

The thermogravimetric (TG) and differential scanning calorimetry (DSC) data were obtained using a NETZSCH STA 499-C thermal analyzer (Germany), under an O_2/Ar stream (flow rate of 30 mL/min) with a heating rate of 10 °C/min from 50 to 600 °C. The sample tested includes Au/γ-Fe_2O_3-Dealloyed.

The microstructure images of the materials were observed using a JSM-7000F field emission scanning electron microscope (SEM, Japan) with an acceleration voltage of 15 kV, and a Japan JEOL JSM-200 transmission electron microscope (TEM, Japan) with an acceleration voltage of 200 kV. The element content of the samples was determined using an INCA X-Sight Oxford energy-dispersive X-ray (EDX) spectrometer. The samples tested include fresh Au/γ-Fe_2O_3-400 and long-term use Au/γ-Fe_2O_3-400.

The N_2 adsorption and desorption measurements to determine the pore structure of the sample were performed on a Micromeritics ASAP 2020 analyzer at -196 °C. Before the analysis, the sample was degassed under vacuum at 130 °C for 12 hours to remove impurities. The specific surface area of the sample was calculated using the Brunauer-Emmett-Teller (BET) method. The pore size distribution of the sample was generated using the Barrett-Joyner-Halenda (BJH) model. The sample tested includes Au/γ-Fe_2O_3-400.

The sample's H_2-temperature programmed reduction (H_2-TPR) was performed on a Micromeritics AutoChem II 2920 instrument equipped with a thermal conductivity detector (TCD). Prior to the TPR run, a 50 mg sample was placed in a U-shaped quartz reactor, pretreated in He flow (60 mL/min) at 200 °C for 1 hour, and then cooled down to 50 °C in the He flow. The treated sample was heated from 50 to 800 °C at a rate of 10 °C/min under a 10 vol.% H_2/Ar gas flow (30 mL/min). Finally, the corresponding data were recorded by TCD. The H_2 consumption of the sample is

calculated by quantitative reduction of a given quantity of CuO to metallic copper. The samples tested include Au/γ-Fe$_2$O$_3$-400 and γ-Fe$_2$O$_3$-400.

The sample's O$_2$-temperature programmed desorption (O$_2$-TPD) was also carried out on the Micromeritics AutoChem II 2920 instrument. A 50 mg of the sample was pretreated under He flow at 300 °C for 1 hour, then cooled down to room temperature under a continuous flow of pure He. Afterward, the sample was pretreated in an O$_2$/Ar gas flow for 1 hour to adsorb oxygen. Finally, the sample was heated to 700 °C at a rate of 10 °C·min^{-1} under pure Ar gas flow with a TCD to record the desorbed oxygen. The samples tested include Au/γ-Fe$_2$O$_3$-400 and γ-Fe$_2$O$_3$-400.

The X-ray photoelectron spectroscopic (XPS) data of the samples were collected with an Axis Ultra Kratos (UK) multifunctional spectrometer using Al Kα radiation (hν = 1486.6 eV) at an ultra-high vacuum. The binding energy of C 1s at 284.8 eV was used for charge correction. The samples tested include Au/γ-Fe$_2$O$_3$-400 and γ-Fe$_2$O$_3$-400.

The Calculation of Activation Energy

The experiment was still carried out on the same tubular continuous-flow fixed-bed quartz reactor as for the catalytic activity tests. 20 mg of catalyst was weighed and mixed thoroughly with quartz wool to equilibrate the volume of the catalytic bed. The mixture was then loaded into the reactor and a gas mixture consisting of CO, O$_2$, and N$_2$ was flowed through at a rate of 120 mL/min. The CO content before and after passing through the reactor at different temperatures was measured using gas chromatography.

For the reaction rate of the catalyst, we calculate it by Eq. (S1):

$$r_{CO} = \frac{N_{CO} \times X}{W_{cat}} \tag{S1}$$

where N_{CO} is the CO molar gas flow rate in mol/s, X is the CO conversion, W_{cat} is the catalyst weight in g, and r_{CO} is the reaction rate.

The activation energy of the Au/γ-Fe$_2$O$_3$-400 catalyst (CO conversion below 15%) was generated from the Arrhenius equation and plot.
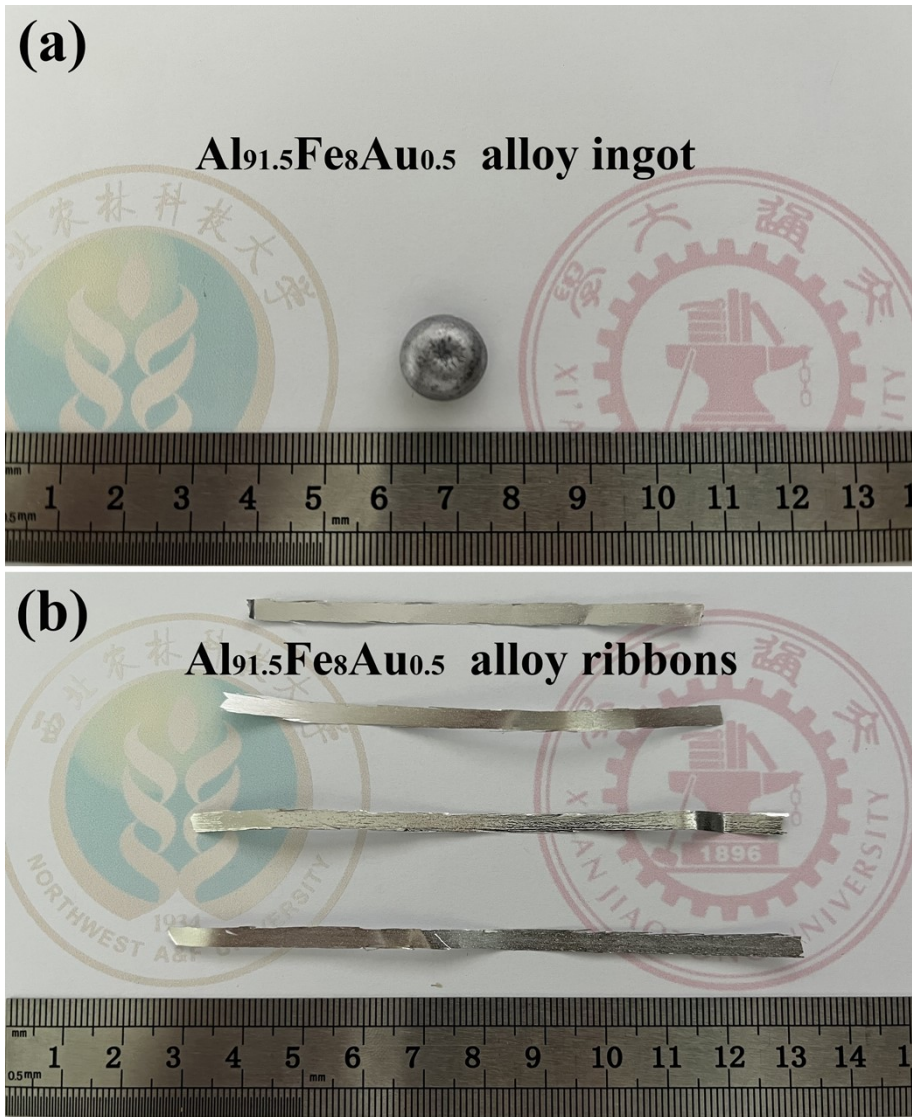
Fig. S1 Optical photos of the $Al_{91.5}Fe_8Au_{0.5}$ alloy ingot (a) and alloy ribbons (b).

Fig. S2 Optical photo of the dealloyed $Al_{92}Fe_8$ sample.

The following auxiliary experiment was designed to further investigate the form in which the Fe element exists during the dealloying process. The Au-free $Al_{92}Fe_8$ alloy ribbon was dealloyed in a 10 wt.% NaOH solution for 12 h at room temperature, hoping to discriminate the sample by the color of the product while excluding the local surface plasmon resonance effect of nanoscale Au from interfering with the experiment. At the end of the dealloying process, the products in the NaOH solution exhibited interlocking white and yellowish-brown colors, as shown in Fig. S2. It is well known that Fe_3O_4 and γ-Fe_2O_3 are black and reddish-brown, respectively. Therefore, the product after dealloying could not be either Fe_3O_4 or γ-Fe_2O_3.[1, 2] The following reasonable conjecture was made: when the Al-Fe alloy was dealloyed in an alkaline solution, the remaining Fe atoms were exposed to the OH- environment due to the selective corrosion of Al by the alkaline solution. These low-coordinated fresh Fe atoms were extremely active and instantly bound to OH-, generating the corresponding hydroxide. In summary, we believe that the white product after dealloying is $Fe(OH)_2$.[3] Since $Fe(OH)_2$ is extremely unstable, even a trace amount of dissolved oxygen in the solution can partially oxidize its surface to the yellowish-brown FeOOH.[4, 5] This observation is consistent with the optical photograph in Fig. S2.
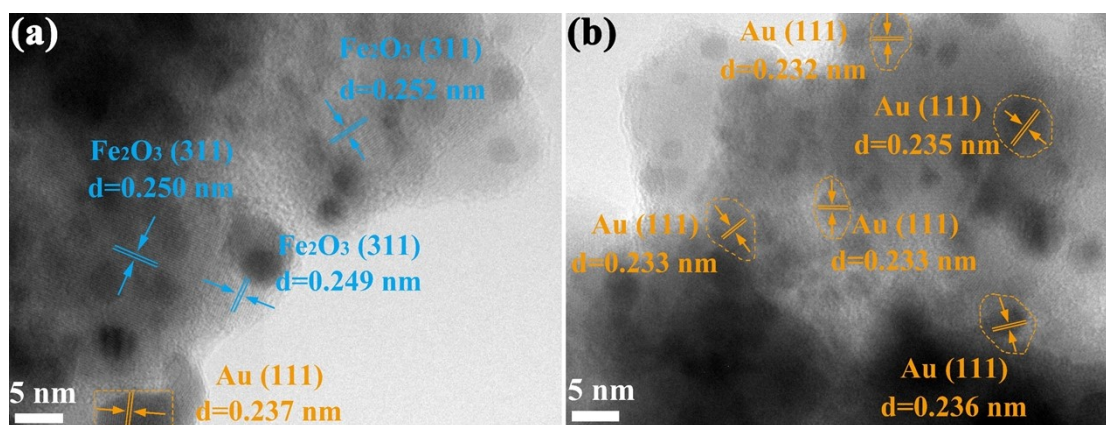
Fig. S3 HRTEM images of the Au/γ-Fe₂O₃-400 catalyst.
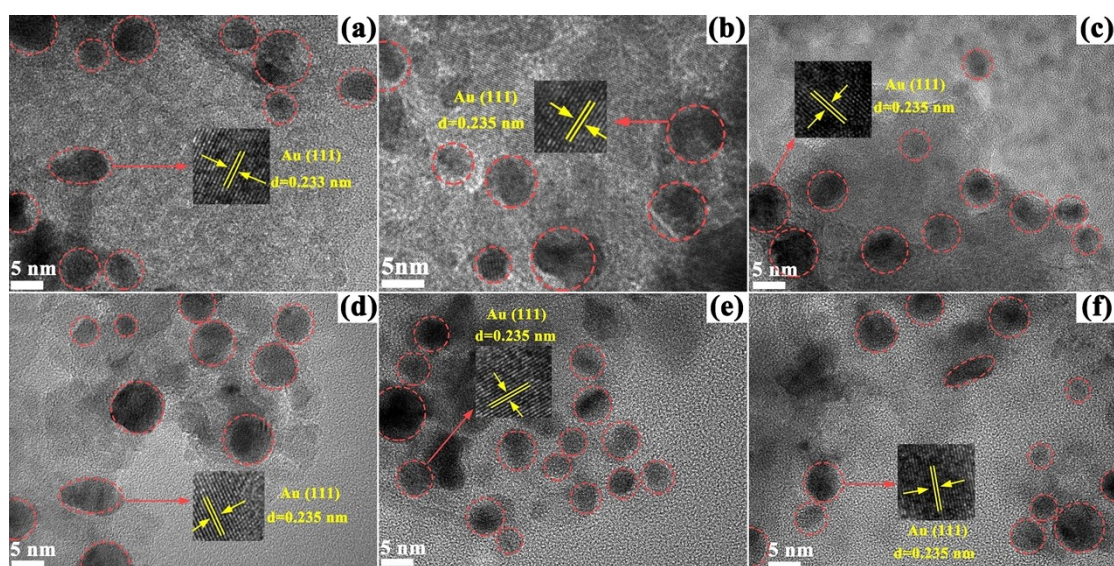

Fig. S4 The HRTEM micrographs of fresh Au/γ-Fe₂O₃-400 (a, b, c) and long-term used Au/γ-Fe₂O₃-400 (d, e, f).

Table S1 The average size of Au nanoparticles over fresh Au/γ-Fe₂O₃-400 and long-term used Au/γ-Fe₂O₃-400.

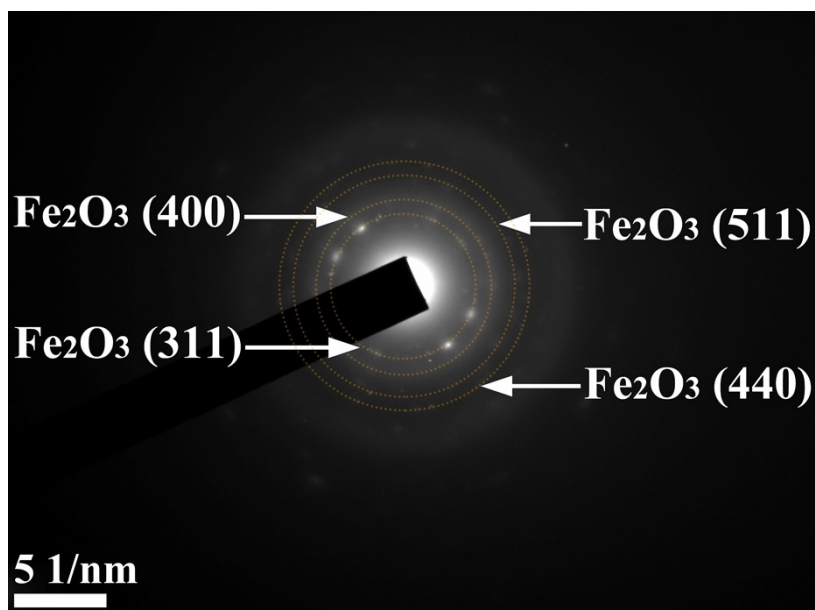| Sample	The average size of Au nanoparticles (nm) [*]	
	Fresh sample	Used sample
Au/γ-Fe₂O₃-400	5.79	5.67

[*] Measurements from Fig. S4.

Fig. S5 SAED pattern of the Au/γ-Fe$_2$O$_3$-400 catalyst.

H$_2$-TPR discussion

The H$_2$ consumption to reduce the cationic Au on the surface depends on the actual cationic Au content on the surface. Here, we consider an extreme case in which all Au is assumed to be distributed on the surface of the catalyst, and is completely oxidized to cationic Au$^+$. The theoretical H$_2$ consumption for the reduction of the surface cation Au is about 122 μmol/g$_{cat}$ (2Au$^+$+H$_2$→2Au+2H$^+$), which is still much smaller than the actual H$_2$ consumption (397 μmol/g$_{cat}$) of the P$_1$ peak of the Au/γ-Fe$_2$O$_3$. In fact, it is unlikely that all of the Au is distributed on the surface of the catalyst, and the results of the XPS analysis (Fig. 5(d)) indicate that only about 16% of the Au on the surface is oxidized to cationic Au. Based on the above analyses, it can be concluded that the actual H$_2$ consumption of the P$_1$ peak is significantly higher than the theoretical amount required for the reduction of surface cationic Au species.
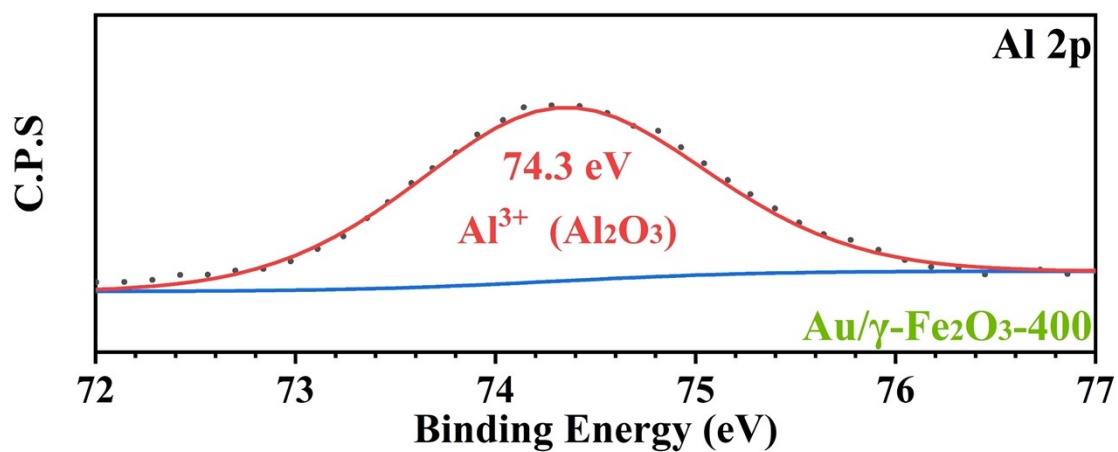
Fig. S6 High-resolution Al $2p$ XPS spectrum of the Au/γ-Fe$_2$O$_3$ catalyst.
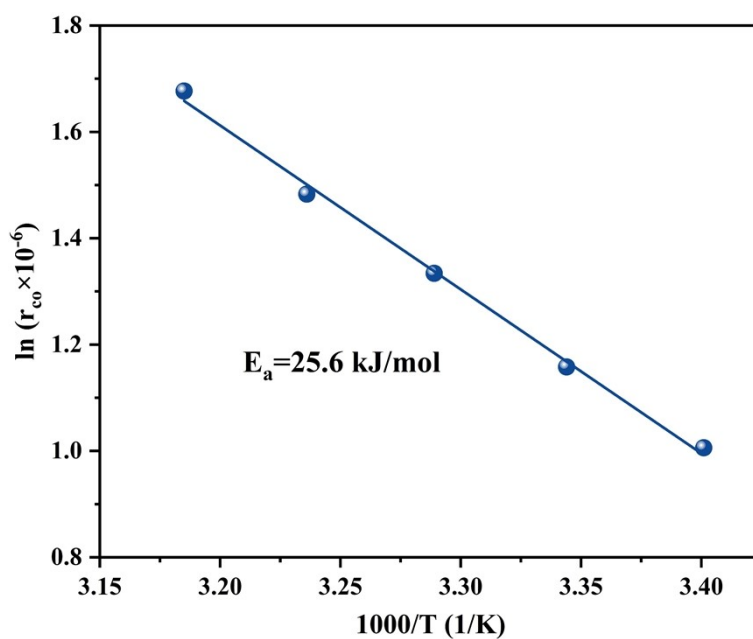

Fig. S7 The Arrhenius plot for CO oxidation over Au/γ-Fe$_2$O$_3$-400 catalyst.

Table S2 The catalytic activities of the recently reported Au/FeO$_X$ catalysts for CO oxidation at low temperatures.

Catalysts	Methods	Au (%)	feed gases (CO:O$_2$)	WHSV (h^{-1})	Conversion temperature (°C)		Reference
					T$_{50}$	T$_{99}$	
Au-FeO$_X$/TiO$_2$	Deposition-precipitation with urea	3.10	1:1	60000	5	75	[6]
Au/FeOOH	Urea coprecipitation	1.90	1:21	1800	40	80	[7]
Au@Fe$_2$O$_3$	One-pot and encapsulation	20.00	1:21	30000	40	75	[8]
Au/Fe$_2$O$_3$	Deposition-precipitation	7.90	/	/	48	250	[9]
Au/Fe$_3$O$_4$/TiO$_2$	Incipient wetness impregnation	/	1:1	102000	180	/	[10]
Au/Fe_OH	Colloidal deposition.	0.98	1:20	80000	-10	50	[11]
Au/α-Fe$_2$O$_3$	Deposition-precipitation	0.89	1:20	80000	0	30	[11]
Au/α-Fe$_2$O$_3$	Double impregnation	1.00	1:2	15000	40	150	[12]
Au–γ-Fe$_2$O$_3$	self-assembly and controlled calcination	/	1:20	/	85	120	[13]
Au/α-Fe$_2$O$_3$ (Spindles)	Colloidal deposition	2.04	1:10	30000	77	150	[14]
Au/α-Fe$_2$O$_3$ (Rods)	Colloidal	2.01	1:10	30000	98	150	[14]

	deposition						
Au/α-Fe$_2$O$_3$ (Hollows)	Colloidal deposition	2.05	1:10	30000	62	83	[14]
Au/α-Fe$_2$O$_3$ (Hollow-rods)	Colloidal deposition	2.02	1:10	30000	82	100	[14]
Au/γ-Fe$_2$O$_3$	deposition–precipitation	1:1	2.9	80000	-30	-20	[15]
Au/α-Fe$_2$O$_3$	deposition–precipitation	1:1	2.9	80000	25	60	[15]
Au/FeO$_X$	Adsorption method.	0.09	1:1	25000	/	50	[16]
Au/γ-Fe$_2$O$_3$	Dealloying combined with calcination	5.81	1:10	30000	/	50	This work

Table S3 The activation energies of the recently reported Au/FeO$_X$ catalysts for CO oxidation.

Catalysts	Methods	Au (%)	Activation energy (kJ/mol)	Reference
Au/γ-Fe$_2$O$_3$ (2.4 wt DP)	Deposition-precipitation	1.3	28	[17]
Au/γ-Fe$_2$O$_3$ (1.2wt SG)	Solid grinding	1.2	30	[17]
Au/α-Fe$_2$O$_3$ (spindles)	Colloidal deposition	2.04	77.57	[14]
Au/α-Fe$_2$O$_3$ (rods)	Colloidal deposition	2.01	65.86	[14]
Au/α-Fe$_2$O$_3$ (hollows)	Colloidal deposition	2.05	51.65	[14]
Au/α-Fe$_2$O$_3$ (hollow-rods)	Colloidal deposition	2.02	53.26	[14]
Au/α-Fe$_2$O$_3$ (Sphere)	Deposition-precipitation	1.01	21.3	[18]
Au/α-Fe$_2$O$_3$ (Rod)	Deposition-precipitation	1.03	20.8	[18]
Au/Fe$_2$O$_3$ (Spongy-8A)	Deposition-precipitation	/	24.44	[19]
Au/Fe$_2$O$_3$ (Spongy-10)	Deposition-precipitation	1.0	39.67	[19]
Au/Fe$_2$O$_3$ (Non-spongy-10)	Deposition-precipitation	0.6	48.05	[19]
Au/FeO$_x$ (CP-1)	Co-precipitation	6	26	[20]
Au/FeO$_x$(CP-2)	Co-precipitation	3.5	30	[20]
Au/Fe$_2$O$_3$	Co-precipitation	/	27	[21]
Au/Fe$_2$O$_3$	Deposition-precipitation	/	29	[22]
Au/Fe$_2$O$_3$	Deposition-precipitation	/	35	[23]
Au/γ-Fe$_2$O$_3$	Dealloying combined with calcination	5.81	25.6	This work

References

1. Q. Han, Liu, Xu, Chen, Wang and H. Zhang, *J. Phys. Chem. C*, 2007, **111**, 5034-5038.
2. R. Ianoş, E. A. Tăculescu, C. Păcurariu and D. Niznansky, *Mater. Chem. Phys.*, 2014, **148**, 705-711.
3. H. Song, X. Ou, B. Han, H. Deng, W. Zhang, C. Tian, C. Cai, A. Lu, Z. Lin and L. Chai, *Angew. Chem. Int. Edit.*, 2021, **60**, 24054-24058.
4. M. Yan, C. Sun, J. Xu, J. Dong and W. Ke, *Corros. Sci.*, 2014, **80**, 309-317.
5. X. Wu, M. Yuan, X. Guo and L. Zhang, *ACS Sustainable Chem. Eng.*, 2019, **7**, 15939-15947.

6. N. S. Portillo-Vélez and R. Zanella, *Chem. Eng. J*, 2020, **385**, 123848.

7. W. Shi, T. Gao, L. Zhang, Y. Ma, Z. Liu and B. Zhang, *Chinese J. Catal.*, 2019, **40**, 1884-1894.

8. M. Lukosi, C. Tian, X. Li, S. M. Mahurin, H. M. Meyer, G. S. Foo and S. Dai, *Catal. Lett.*, 2018, **148**, 2315-2324.

9. S. Tanaka, J. Lin, Y. V. Kaneti, S. I. Yusa, Y. Jikihara, T. Nakayama, M. B. Zakaria, A. A. Alshehri, J. You, M. S. A. Hossain and Y. Yamauchi, *Nanoscale*, 2018, **10**, 4779-4785.

10. S. Gaur, S. Johansson, F. Mohammad, C. S. S. R. Kumar and J. J. Spivey, *J. Phys. Chem. C*, 2012, **116**, 22319-22326.

11. Y. Guo, D. Gu, Z. Jin, P. P. Du, R. Si, J. Tao, W. Q. Xu, Y. Y. Huang, S. Senanayake, Q. S. Song, C. J. Jia and F. Schüth, *Nanoscale*, 2015, **7**, 4920-4928.

12. S. A. C. Carabineiro, N. Bogdanchikova, P. B. Tavares and J. L. Figueiredo, *RSC Adv.*, 2012, **2**, 2957-2965.

13. L. Shang, Y. Liang, M. Li, G. I. N. Waterhouse, P. Tang, D. Ma, L. Z. Wu, C. H. Tung and T. Zhang, *Adv. Funct. Mater.*, 2017, **27**, 1606215.

14. L. Zeng, K. Li, H. Wang, H. Yu, X. Zhu, Y. Wei, P. Ning, C. Shi and Y. Luo, *J. Phys. Chem C*, 2017, **121**, 12696-12710.

15. K. Zhao, H. Tang, B. Qiao, L. Li and J. Wang, *ACS Catal.*, 2015, **5**, 3528-3539.

16. B. Qiao, J. X. Liang, A. Wang, C. Q. Xu, J. Li, T. Zhang and J. J. Liu, *Nano Res.*, 2015, **8**, 2913-2924.

17. T. Akita, Y. Maeda and M. Kohyama, *J. Catal.*, 2015, **324**, 127-132.

18. Y. Gao, F. K. Chiang, S. Li, L. Zhang, P. Wang and E. J. M. Hensen, *Chinese J. Catal.*, 2021, **42**, 658-665.

19. B. Sarkodie, B. Shen, B. Asinyo, Y. Hu, J. Jiang and C. Li, *J. Colloid Interf. Sci.*, 2022, **608**, 2181-2191.

20. Q. He, S. J. Freakley, J. K. Edwards, A. F. Carley, A. Y. Borisevich, Y. Mineo, M. Haruta, G. J. Hutchings and C. J. Kiely, *Nat. Commun.*, 2016, **7**, 12905.

21. A. Y. Klyushin, M. T. Greiner, X. Huang, T. Lunkenbein, X. Li, O. Timpe, M. Friedrich, M. Hävecker, A. Knop-Gericke and R. Schlögl, *ACS Catal.*, 2016, **6**, 3372-3380.

22. M. M. Schubert, S. Hackenberg, A. C. van Veen, M. Muhler, V. Plzak and R. J. Behm, *J. Catal.*, 2001, **197**, 113-122.

23. M. Haruta, S. Tsubota, T. Kobayashi, H. Kageyama, M. J. Genet and B. Delmon, *J. Catal.*, 1993, **144**, 175-192.